

Modulation of the anomalous Hall angle in a magnetic topological semimetal

Received: 28 March 2024

Accepted: 25 February 2025

Published online: 02 April 2025

 Check for updates

Jinying Yang^{1,2}, Yanxing Shang¹, Xingchen Liu^{1,2}, Yiibo Wang^{1,2}, Xuebin Dong^{1,2}, Qingqi Zeng¹, Meng Lyu¹, Shen Zhang¹, Yang Liu^{1,2}, Binbin Wang¹, Hongxiang Wei¹, Yizheng Wu³, Stuart Parkin⁴, Gangqin Liu¹, Claudia Felser⁵, Enke Liu¹✉ & Baogen Shen^{1,6}

The anomalous Hall angle (θ^A) is a measure of the efficiency of converting a longitudinal driving current into a transverse spin-polarized Hall current. In sensors based on the anomalous Hall effect, a large anomalous Hall angle can improve the sensitivity of magnetic field detection. However, the modulation of this angle is challenging, and magnetic materials typically have low angles of 0.1° – 3° . Here we report the modulation of θ^A in the magnetic Weyl semimetal $\text{Co}_3\text{Sn}_2\text{S}_2$. We show that the anomalous Hall angle parameter $\tan\theta^A$ can be formulated as a function of the product of electrical resistivity and anomalous Hall conductivity. We use this scheme to demonstrate the modulation of $\tan\theta^A$ up to a magnitude of 0.46, corresponding to an angle of around 25° . We further fabricate anomalous Hall devices using Fe-doped $\text{Co}_3\text{Sn}_2\text{S}_2$ single-crystalline nanoflakes and demonstrate a Hall sensitivity of $7,028 \pm 341 \mu\Omega \text{ cm T}^{-1}$ and a magnetic field detectability of $23.5 \pm 1.7 \text{ nT Hz}^{-0.5}$ at 1 Hz.

The anomalous Hall effect (AHE) arises from an intrinsic mechanism connected to the Berry curvature of electronic bands and an extrinsic contribution from the scattering effects of impurities^{1–3}. An essential parameter of the AHE is $\tan\theta^A = \sigma_H^A/\sigma_{xx}$ (anomalous Hall conductivity (AHC)/longitudinal conductivity), which represents the conversion efficiency of the longitudinal electric current density to the anomalous Hall current density. Here θ^A (the anomalous Hall angle) is the angle between the total current density (j) and the driving current density (j_x) (Fig. 1a). A large θ^A corresponds to a large anomalous Hall current. It is expected that materials with a large $\tan\theta^A$ and high spin polarization can generate large spin anomalous Hall angles⁴, which makes the AHE an efficient spin current source for spin transfer torque^{4,5}. In cases of anomalous Hall sensors, a large θ^A improves the sensitivity of magnetic field detection^{6–8}.

In most magnetic materials, the magnitude of $\tan\theta^A$ (or θ^A) is below 0.05 (or 3°). Thus, the $\tan\theta^A$ value of materials used in anomalous Hall sensors is small. For example, the $\tan\theta^A$ value of $\text{Co}_{40}\text{Fe}_{40}\text{B}_{20}$ is 0.007

(ref. 7) and the $\tan\theta^A$ value of $\text{Fe}_{0.48}\text{Pt}_{0.52}$ is 0.020 (ref. 6). Therefore, the AHE has had few technological applications so far. Compared with conventional magnetic materials, topological magnets with Weyl fermions and a strong Berry curvature exhibit a large AHE and $\tan\theta^A$ (refs. 9–12). Some studies have reported the effects of doping on the AHC and an enhanced $\tan\theta^A$ (refs. 13–15). However, prior studies have typically focused on the relation between the topological band structure and the AHC. Furthermore, the modulation scheme and underlying rules of $\tan\theta^A$ have not been systematically investigated.

In this Article, we report the modulation of θ^A in a magnetic topological material. We establish a relation between $\tan\theta^A$, longitudinal resistivity (ρ_{xx}) and σ_H^A , and demonstrate the modulation of $\tan\theta^A$ up to a magnitude of 0.46 (corresponding to θ^A of around 25°) in the magnetic Weyl semimetal $\text{Co}_3\text{Sn}_2\text{S}_2$. We also use Fe-doped $\text{Co}_3\text{Sn}_2\text{S}_2$ single-crystalline nanoflakes to fabricate anomalous Hall devices, which demonstrate a Hall sensitivity of $7,028 \pm 341 \mu\Omega \text{ cm T}^{-1}$ and a magnetic field detectability of $23.5 \pm 1.7 \text{ nT Hz}^{-0.5}$ at 1 Hz.

¹Beijing National Laboratory for Condensed Matter Physics, Institute of Physics, Chinese Academy of Sciences, Beijing, China. ²School of Physical Sciences, University of Chinese Academy of Sciences, Beijing, China. ³Department of Physics and State Key Laboratory of Surface Physics, Fudan University, Shanghai, China. ⁴Max Planck Institute of Microstructure Physics, Halle, Germany. ⁵Max Planck Institute for Chemical Physics of Solids, Dresden, Germany. ⁶Ningbo Institute of Materials Technology & Engineering, Chinese Academy of Sciences, Ningbo, China. ✉e-mail: ekliu@iphy.ac.cn

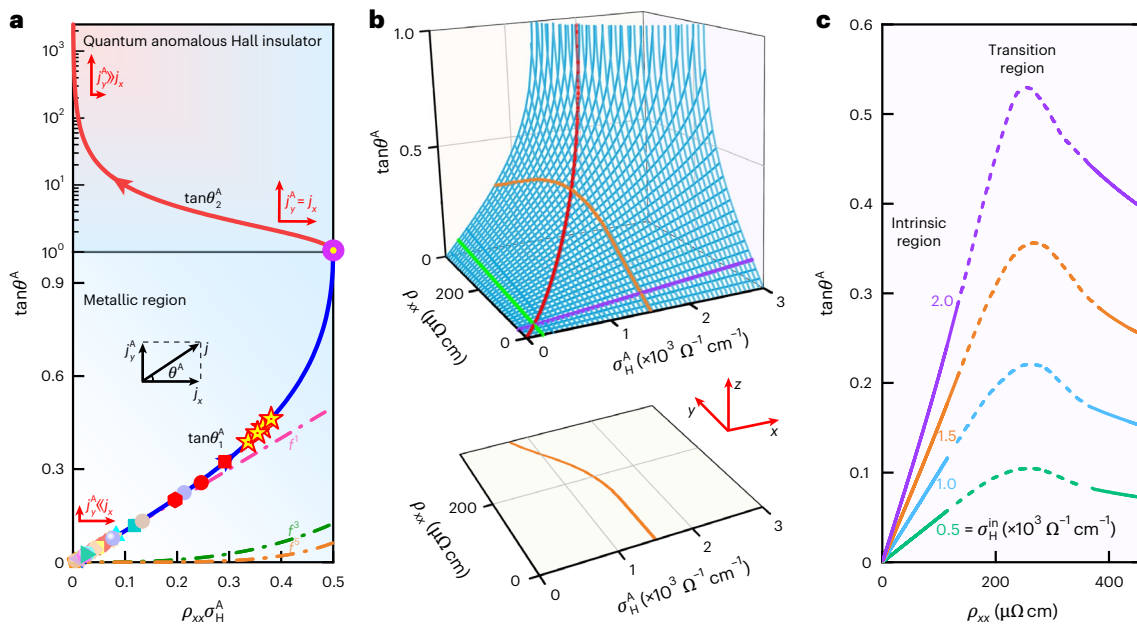


Fig. 1 | Generic formula and scheme for θ^A . **a**, Relation between $\tan\theta^A$, ρ_{xx} and AHC (σ_H^A). The data are shown in Supplementary Table 1. Absolute values of $\tan\theta^A$ and σ_H^A are adopted here. Two solutions (θ_1^A and θ_2^A) connect the two regions, and the split line is $\tan\theta^A = 1$. For most materials, $\tan\theta^A$ is usually smaller than 0.05. The dotted lines indicate the first-order (f^1), third-order (f^3) and fifth-order (f^5) terms of the Taylor expansion. j_y^A and j_x are the anomalous Hall current density and longitudinal current density, respectively. The shading, which changes from white to blue and red, roughly indicates an increase in $\tan\theta^A$. **b**, Three-dimensional plot of $\tan\theta^A$ as a function of ρ_{xx} and σ_H^A . The green (purple) curve represents $\tan\theta^A$ as a function of ρ_{xx} (σ_H^A) when $\sigma_H^A = 180 \Omega^{-1} \text{ cm}^{-1}$ ($\rho_{xx} = 30 \mu\Omega \text{ cm}$).

In both cases, $\tan\theta^A$ increases slowly with increasing σ_H^A (ρ_{xx}) when ρ_{xx} (σ_H^A) is low. In contrast, $\tan\theta^A$ rapidly increases (red curve) when ρ_{xx} and σ_H^A increase simultaneously. The $\tan\theta^A$ value increases with ρ_{xx} along the line of intrinsic $\sigma_H^A = 1,500 \Omega^{-1} \text{ cm}^{-1}$ and then decreases owing to the decay of σ_H^A during parameter tuning (orange curve). The x–y plane projection of the orange curve demonstrates a clear dependence of σ_H^A on ρ_{xx} . **c**, Relation between $\tan\theta^A$ and ρ_{xx} extracted from the y–z plane projection of **b**. The dashed lines in the middle correspond to the transition region from the intrinsic to the hopping region. 0.5, 1.0, 1.5 and 2.0 are the values of intrinsic AHC σ_H^A ($10^3 \Omega^{-1} \text{ cm}^{-1}$) in the intrinsic region.

Physical scheme for tuning $\tan\theta^A$

Among anomalous Hall resistivity (ρ_{xx}), ρ_{xx} , σ_H^A and σ_{xx} , any two parameters are sufficient to determine $\tan\theta^A$ according to the definition and the tensor conversion under the Drude model (Supplementary Section 1.1). The intrinsic and extrinsic skew scattering σ_H^A contributions can be distinguished by the scaling relation^{16,17}. The intrinsic σ_H^A value can be theoretically obtained by calculating the band Berry curvature, whereas the extrinsic component is related to impurity scattering. ρ_{xx} is a fundamental parameter related to scattering and can be measured directly in electrical transport. Therefore, the selection of σ_H^A and ρ_{xx} to express $\tan\theta^A$ has three advantages. (1) Intrinsic σ_H^A and ρ_{xx} can be controlled by independent factors and, thus, modulated explicitly and separately in experiments. (2) The temperature dependence of $\tan\theta^A$ can be predicted by theoretical calculations and resistance measurements for a given material. (3) The simultaneous increase in σ_H^A and ρ_{xx} can be experimentally achieved in a given system. The accurate expression for $\tan\theta^A$ is, thus, formulated as $\tan\theta^A = (1 + \tan^2\theta^A)\rho_{xx}\sigma_H^A$ (Supplementary

Section 1.1). The two solutions ($\tan\theta_1^A = \frac{1 - \sqrt{1 - 4(\rho_{xx}\sigma_H^A)^2}}{2\rho_{xx}\sigma_H^A} \in (0, 1]$ and $\tan\theta_2^A = \frac{1 + \sqrt{1 - 4(\rho_{xx}\sigma_H^A)^2}}{2\rho_{xx}\sigma_H^A} \in [1, +\infty)$) of this quadratic equation show

that $\tan\theta^A$ is a function of the product ($\rho_{xx}\sigma_H^A$) of the longitudinal resistivity (ρ_{xx}) and AHC (σ_H^A). The relation between $\tan\theta^A$ and $\rho_{xx}\sigma_H^A$ is plotted in Fig. 1a.

$\tan\theta^A = 0$ is a limiting case in which the anomalous Hall current is zero. Most magnetic materials with low $\tan\theta^A$ are usually located around here. In this region, the $\tan\theta_1^A$ value increases monotonously with the increase in $\rho_{xx}\sigma_H^A$. The larger $\rho_{xx}\sigma_H^A$ is, the more the high-order terms of the Taylor expansion contribute to $\tan\theta^A$ (Supplementary Fig. 4),

Table 1 | Different cases for tuning $\tan\theta^A$

Case	σ_H^A	ρ_{xx}	$\sigma_H^A\rho_{xx}$	$\tan\theta^A$	Approaches
I	↓	↑	↑	↑	
II-1	→	↑	↑	↑↑	Co ₃ Sn ₂ S ₂ (intrinsic, temperature (T), thickness (t))
II-2	↑	→	↑	↑↑	
III	↑	↑	↑	↑↑↑	Fe-doped Co ₃ Sn ₂ S ₂ (intrinsic+extrinsic, doping)
IV	↑	↓	↑	↑	Extrapolation using Tian–Ye–Jin model ¹⁶ (extrinsic+intrinsic)

↑, ↓ and → represent an increase, decrease and invariability of parameters, respectively. More arrows mean faster increase. $\tan\theta^A$ is tuned as a function of $\rho_{xx}\sigma_H^A$.

which makes $\tan\theta_1^A$ increase rapidly when $\rho_{xx}\sigma_H^A$ exceeds 0.3. When $\rho_{xx}\sigma_H^A$ reaches 0.5, the two solutions meet at 1 ($\theta^A = 45^\circ$), where the anomalous Hall current density equals the longitudinal one. After $\tan\theta_1^A$ exceeds 1, it continues to increase with decreasing $\rho_{xx}\sigma_H^A$. For the limit at which $\tan\theta_2^A$ approaches infinity, one can expect the quantum anomalous Hall insulating state in a two-dimensional case¹⁸. For the $\tan\theta_1^A$ solution, it dominates the metallic region in which the conducting electrons play a fundamental role in electronic or thermo-electronic transport (Fig. 1a).

Our work primarily focuses on $\tan\theta_1^A$. Figure 1b shows the three-dimensional plot of $\tan\theta^A$ as a function of both ρ_{xx} and σ_H^A , which exhibits a chimney-like distribution of $\tan\theta^A$. As indicated by the green and purple lines, low σ_H^A results in low $\tan\theta^A$, which corresponds to many conventional magnetic materials. Low ρ_{xx} also leads to low $\tan\theta^A$ (Fig. 1b) even for materials with a magnitude of σ_H^A in the thousands, such as Fe and kagome metals^{19,20}. Evidently, the most efficient

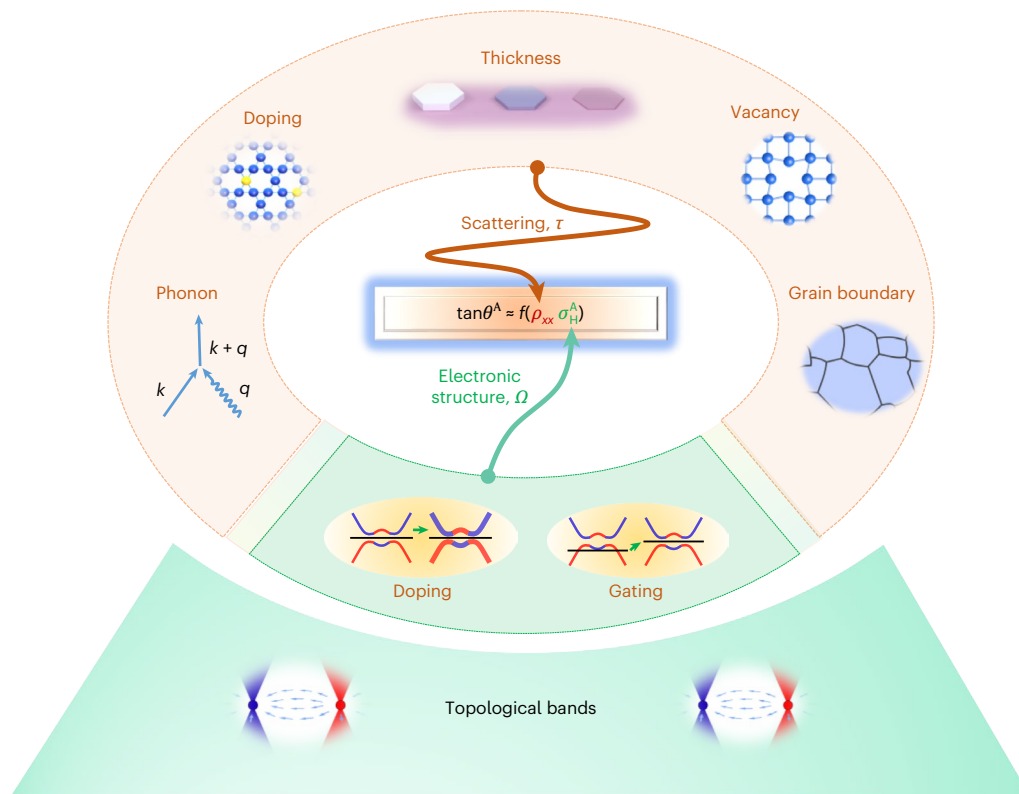


Fig. 2 | Proposed degrees of freedom for tuning $\rho_{xx}\sigma_H^A$ based on topological magnets. As $\tan\theta^A$ is a physical quantity that is related to both intrinsic and extrinsic factors, we analyse the influence of modulation methods on $\tan\theta^A$ from the perspective of the intrinsic band structure and extrinsic scattering. σ_H^A can be modulated by doping and gating, which affects the electronic structure at the

Fermi level and associated Berry curvature (Ω). We can even grasp ρ_{xx} as the single variable to tune $\tan\theta^A$ if using materials with giant intrinsic σ_H^A instead of directly tuning the product variable $\rho_{xx}\sigma_H^A$. The methods for decreasing τ and increasing ρ_{xx} include temperature-dependent scattering, doping, reduced thickness, vacancy and grain boundary.

path to get a large $\tan\theta^A$ is to increase ρ_{xx} and σ_H^A simultaneously (Fig. 1b, red line).

To find out practical experimental methods to achieve large $\tan\theta^A$, we further analyse ρ_{xx} and σ_H^A in real materials (Table 1). Case III is the most efficient approach for obtaining large $\tan\theta^A$, but it needs to be tailored specifically to the material. Previous works suggest that a larger $\tan\theta^A$ could be obtained by extrapolating to the higher-conductivity region using the Tian–Ye–Jin model^{16,19}. However, this method of increasing $\tan\theta^A$ is less efficient because ρ_{xx} largely decreases (case IV). For simplicity, generality and efficiency, considering that the intrinsic σ_H^A and ρ_{xx} can be modulated by independent variables, we analysed the necessary conditions for materials with intrinsic σ_H^A (case II-1).

As an example, we consider the case of intrinsic σ_H^A of $1,500 \Omega^{-1} \text{cm}^{-1}$ (Fig. 1b, orange line). The intrinsic σ_H^A value remains constant if ρ_{xx} increases by external variables without altering the band structure of a given system, and $\tan\theta^A$ increases according to Fig. 1b. σ_H^A decays ($\sigma_H^A \propto \sigma_{xx}^{1.6}$; Supplementary Fig. 7 shows the unified model^{21,22}) if ρ_{xx} increases further into the hopping region, resulting in a decrease in $\tan\theta^A$. A maximum of $\tan\theta^A$ can be obtained at the transition region connecting the intrinsic and hopping regions. The relation between σ_H^A ($\tan\theta^A$) and ρ_{xx} can be deduced from Fig. 1b, as shown in the projection of the x - y plane (y - z plane) in Fig. 1b (Fig. 1c). Additional curves with intrinsic σ_H^A are presented in Supplementary Fig. 6 and Fig. 1c.

The transition region is located across a range (for example, 150–350 $\mu\Omega \text{cm}$), which depends on the materials and modulating approaches. For a given material system, to obtain large $\tan\theta^A$, the intrinsic region should be as wide as possible before ρ_{xx} enters the transition region. Figure 1c shows that for larger values of intrinsic σ_H^A , the maximum of $\tan\theta^A$ increases in the transition region.

Modulation scheme with designed degrees of freedom

The determination of the degrees of freedom is essential for the experimental realization of large $\tan\theta^A$. For simplicity, we start from the modulation of a single variable and give selected approaches based on the nature of intrinsic σ_H^A and ρ_{xx} . Clearly, the fastest way to increase $\tan\theta^A$ is to simultaneously increase both σ_H^A and ρ_{xx} (Fig. 1b, red line). As tuning approaches often have various effects on the material properties, proper experimental approaches are required to achieve this simultaneous increase in σ_H^A and ρ_{xx} . Therefore, different degrees of freedom that closely correlate ρ_{xx} and σ_H^A were proposed for this design (Fig. 2).

In the case of the modulation of intrinsic σ_H^A , the intrinsic σ_H^A is determined by the electronic band structure, which is affected by the crystal field, exchange interaction and spin–orbital coupling of a system²³. When the Fermi level is tuned into the spin–orbital-coupling-opened anti-crossing gap in a topological magnet, the intrinsic σ_H^A will be enhanced resonantly^{3,9,21}. This can be experimentally achieved by gating, electron doping or hole doping^{13–15,18,24}.

In the case of the modulation of ρ_{xx} , the large Berry curvature around the Fermi level is always obtained in topological magnets^{9–11,25}. Furthermore, on the basis of the large intrinsic σ_H^A , the thickness t (refs. 16,26,27), temperature (T)-dependent factors (electron–electron²⁸, electron–phonon²⁹ and electron–magnon³⁰ interactions), doping, vacancy or grain boundary are potential scattering modalities, which alter the relaxation time (τ). Modulating ρ_{xx} without significantly altering the electronic band structures corresponds to case II-1 in Table 1. $\tan\theta^A$ will increase with the decrease (or increase) in the variables (t , T , concentrations of vacancy or grain boundary).

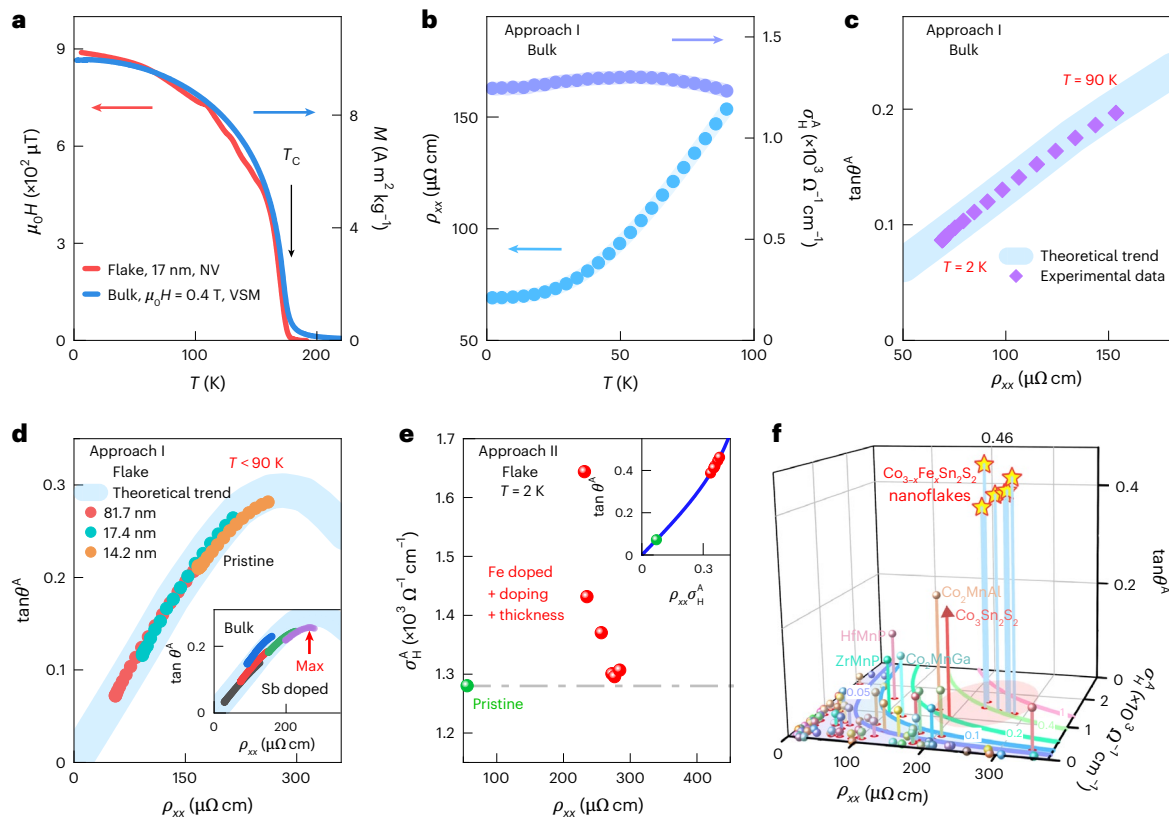


Fig. 3 | Experimental modulations of θ^A in $\text{Co}_3\text{Sn}_2\text{S}_2$. **a**, Temperature (T) dependence of the magnetization (M) of $\text{Co}_3\text{Sn}_2\text{S}_2$ bulk at 0.4 T measured using a vibrating sample magnetometer (VSM). The local magnetic field ($\mu_0 H$) is detected by the NV sensors, which is proportional to the stray field of the $\text{Co}_3\text{Sn}_2\text{S}_2$ nanoflake sample with a thickness of 17 nm in zero field. The bulks and flakes have a consistent Curie temperature (T_C) at 175 K. **b**, Temperature dependencies of ρ_{xx} and σ_H^A of $\text{Co}_3\text{Sn}_2\text{S}_2$ bulks at 0.4 T. **c**, Increase in $\tan\theta^A$ induced by the increase in ρ_{xx} as the temperature increases up to 90 K at 0.4 T. **d**, $\tan\theta^A$ of $\text{Co}_3\text{Sn}_2\text{S}_2$ nanoflakes with different thicknesses measured at 0.1 T below 90 K (pink, 81.7 nm; cyan, 17.4 nm; orange, 14.2 nm). The inset shows the ρ_{xx} -dependent $\tan\theta^A$ of $\text{Co}_3\text{Sn}_2\text{S}_2$ bulks (black, red, blue, green and purple curves correspond to $y = 0, y = 0.1, y = 0.3, y = 0.5$ and $y = 0.7$, respectively)¹⁵. **e**, Enhanced

ρ_{xx} and σ_H^A by decreasing the thickness and Fe doping (green, pristine flake with a thickness of 81.7 nm; red, Fe-doped flakes). The inset shows the σ_H^A - ρ_{xx} dependence of $\tan\theta^A$ of the $\text{Co}_3\text{Sn}_2\text{S}_2$ nanoflake and Fe-doped $\text{Co}_3\text{Sn}_2\text{S}_2$ nanoflakes. The Hall loop, thickness and level of Fe doping are shown in Supplementary Fig. 18. The grey dotted line is σ_H^A of the pristine $\text{Co}_3\text{Sn}_2\text{S}_2$ flake with a thickness of 81.7 nm. The blue line in the inset is the curve of θ_1^A in Fig. 1a. **f**, Enhancement of $\tan\theta^A$ at 2 K by doping and surface scattering (the red-yellow pentagrams denote Fe-doped nanoflakes). Comparison of $\tan\theta^A$ between previous reports and our results. The red triangle represents the pristine $\text{Co}_3\text{Sn}_2\text{S}_2$ (ref. 9) bulk. The contour lines in the ρ_{xx} - σ_H^A plane represent $\tan\theta^A$. Information about the materials is presented in Supplementary Table 1.

In the case of the modulation of both ρ_{xx} and σ_H^A , we note that chemical doping is an experimental method that distinctively affects $\tan\theta^A$ (refs. 13–15). Doping can increase ρ_{xx} by enhancing scattering; simultaneously, it increases transverse σ_H^A by introducing the extrinsic contribution or, even intriguingly, enhancing the intrinsic contribution owing to band broadening or Fermi level shifting^{13,14}. These cases are related to case III in Table 1. In this case, $\tan\theta^A$ may rapidly increase, as expected (Fig. 1b, red line).

Realization of large $\tan\theta^A$ and sensing demonstration

On the basis of our proposed formula and design scheme, we select $\text{Co}_3\text{Sn}_2\text{S}_2$ for our experimental validation. $\text{Co}_3\text{Sn}_2\text{S}_2$ is a typical magnetic Weyl semimetal with giant intrinsic σ_H^A (refs. 9,31). We began with the large intrinsic σ_H^A and engineered the ρ_{xx} value to enter the transition region through temperature-dependent scattering and reduction in the sample thickness. In this case, we obtained a large intrinsic $\tan\theta^A$ for $\text{Co}_3\text{Sn}_2\text{S}_2$. Furthermore, we enhanced $\tan\theta^A$ by introducing extrinsic σ_H^A and increasing ρ_{xx} via Fe doping and decreasing the thickness. Figure 3 shows the experimental results of modulating $\tan\theta^A$ in $\text{Co}_3\text{Sn}_2\text{S}_2$ through different parameters (details of the samples and measurements are provided in Methods and Supplementary

Sections 2 and 3). The temperature-dependent magnetizations for bulks and nanoflakes confirm the robust magnetic order even in the nanoflakes (Fig. 3a).

Temperature is an effective factor that can be easily controlled in experiments. The effects of temperature on σ_H^A and ρ_{xx} of $\text{Co}_3\text{Sn}_2\text{S}_2$ are shown in Fig. 3b. Owing to the stable ferromagnetic state and electronic band structure, the intrinsic σ_H^A is temperature-independent below 90 K (refs. 32,33). However, ρ_{xx} increases significantly with the temperature due to the increase in electron–magnon scattering. Our fitting result is consistent with the results of inelastic neutron scattering³⁴ and electronic transport³⁵ in $\text{Co}_3\text{Sn}_2\text{S}_2$ reported previously (Supplementary Section 2.2.2). In Fig. 3c, $\tan\theta^A$ increases significantly with ρ_{xx} from 2 K to 90 K, which is consistent with Fig. 1c and corresponds to case II-1 in Table 1. This behaviour can also be observed in other systems (Supplementary Fig. 12).

Reducing the thickness of the nanoflake samples is another method to increase ρ_{xx} (refs. 16,27), which can be used to drive ρ_{xx} to enter the transition region for the largest intrinsic $\tan\theta^A$. As ρ_{xx} increases, $\tan\theta^A$ of $\text{Co}_3\text{Sn}_2\text{S}_2$ nanoflakes increases to nearly 0.3 by reducing the thickness and increasing the temperature (Fig. 3d and Supplementary Fig. 16). This behaviour, in which $\tan\theta^A$ exhibits a maximum in the transition region, is also observed in Sb-doped $\text{Co}_3\text{Sn}_2\text{S}_2$ bulks¹⁵

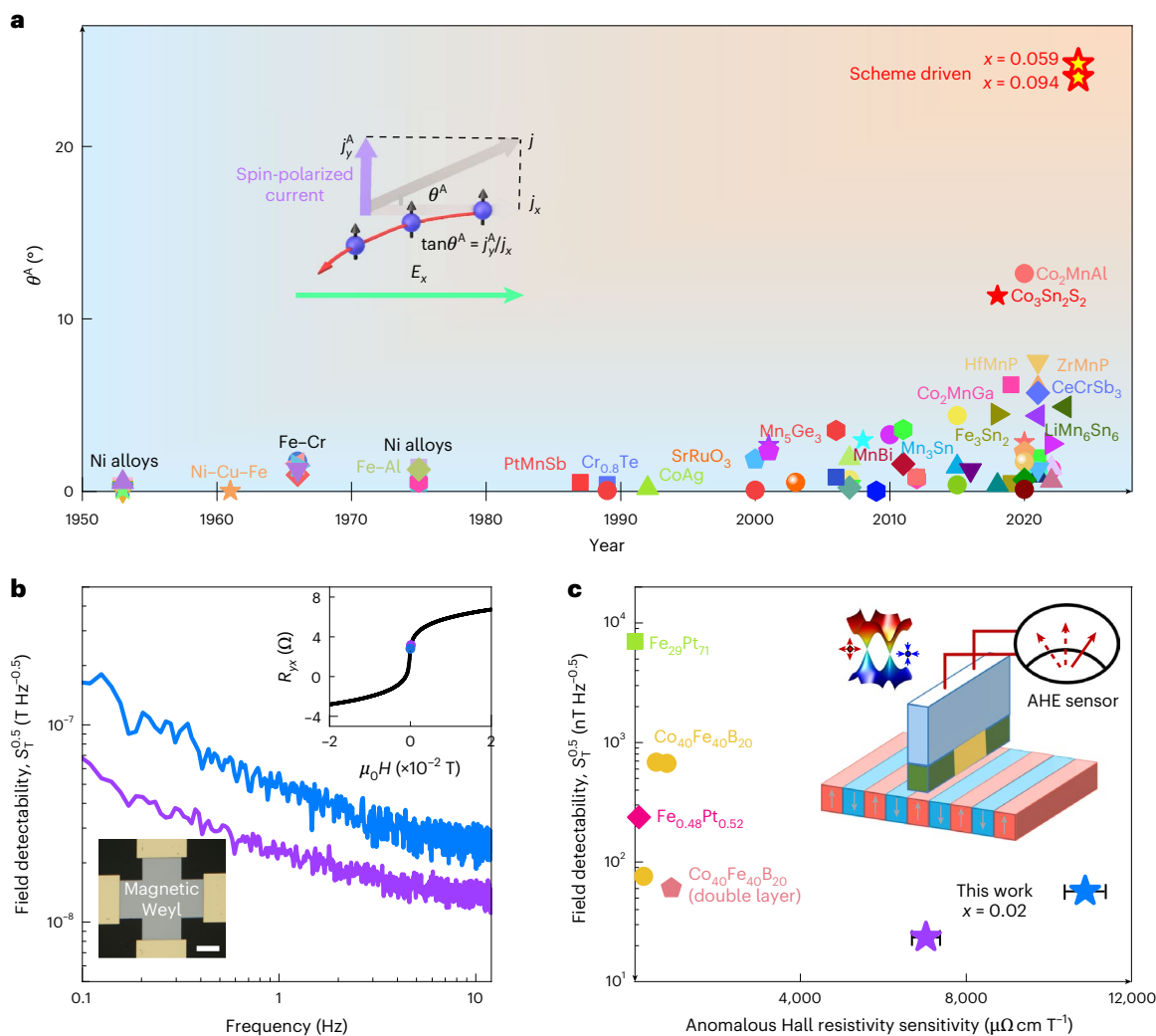


Fig. 4 | Zero-field θ^A and anomalous Hall sensing. **a**, Development of the zero-field θ^A of our results ($\text{Co}_{3-x}\text{Fe}_x\text{Sn}_2\text{S}_2$ nanoflakes) and those of conventional metals. Data from all the materials are shown in Supplementary Table 1. The purple and grey arrows indicate the direction of current density j . The red and blue arrows indicate the direction of electron movement and the direction of longitudinal electric field (E_x), respectively. The shading means an increase in θ^A with year. **b**, Magnetic field detectability ($S_T^{0.5}$) spectra of the $\text{Co}_{2.98}\text{Fe}_{0.02}\text{Sn}_2\text{S}_2$ nanoflake at 173.3 K. The bottom-left inset shows the Hall device. Scale bar, 20 μm . The top-right inset is the transverse resistance and the purple/blue dots are the locations at which the noise spectra were measured (Methods and Supplementary Section 5). The purple/blue curves correspond to the purple/blue dots in the top-right inset. **c**, Distribution of magnetic field detectability (at 1 Hz) and anomalous Hall resistivity sensitivity. The purple and blue stars

correspond to the purple and blue curves in **b**. To exclude the thickness factor of devices, the $\Delta\rho_H^A/\Delta(\mu_0 H)$ value was used to represent the anomalous Hall resistivity sensitivity. The grey and black error bars (standard deviation) are the error bars of $S_T^{0.5}$ and anomalous Hall resistivity sensitivity, respectively. The $S_T^{0.5}$ values are $23.5 \pm 1.7 \text{ nT Hz}^{-0.5}$ (purple) and $57.0 \pm 5.4 \text{ nT Hz}^{-0.5}$ (blue), respectively. The error of $S_T^{0.5}$, calculated using the error propagation formula, arises from the repeated Hall voltage measurements and the linear fitting of the field-dependent anomalous Hall resistance. Even near the Curie temperature of the nanoflakes, the advantage of materials with large θ^A in magnetic field detection is demonstrated. The results of $\text{Fe}_{0.48}\text{Pt}_{0.52}$, $\text{Co}_{40}\text{Fe}_{40}\text{B}_{20}$ (double layer), $\text{Fe}_{29}\text{Pt}_{71}$ and $\text{Co}_{40}\text{Fe}_{40}\text{B}_{20}$ are obtained from refs. 6,7,42,43. The inset shows a schematic of the AHE sensor.

(Fig. 3d, inset), where σ_H^A is primarily dominated by the intrinsic mechanism. This intrinsic approach (case II-1 in Table 1 and Fig. 1c) is, thus, effective and universal for tuning $\tan\theta^A$. Therefore, for a material with an intrinsic σ_H^A , the T -dependent (or other parameters-dependent) $\tan\theta^A$ can be predicted if the correspondence between ρ_{xx} and T (or other parameters) is obtained. This is advantageous for the film device applications of θ^A , where the maximum $\tan\theta^A$ and excellent properties can be obtained around the working temperature in a suitable thickness for the materials.

Fe-doped $\text{Co}_3\text{Sn}_2\text{S}_2$ nanoflakes were studied as another approach to increase the product of σ_H^A and ρ_{xx} . Owing to the increase in doping level and decrease in thickness, ρ_{xx} at 2 K increases to 200–300 $\mu\Omega \text{ cm}$ (Fig. 3e), whereas σ_H^A remains at a high level of approximately 1,300 $\Omega^{-1} \text{ cm}^{-1}$ and can reach even higher values up to 1,600 $\Omega^{-1} \text{ cm}^{-1}$

(Fig. 3e). The components of σ_H^A cannot be separated by the Tian–Ye–Jin model¹⁶ because ρ_{xx} enters the transition region (Supplementary Fig. 18d) and the intrinsic σ_H^A value is not constant anymore. By comparing the $\tan\theta^A$ – ρ_{xx} curves of Fe-doped $\text{Co}_3\text{Sn}_2\text{S}_2$ nanoflakes with that of the intrinsic theoretical trend, it was found that the extrinsic skew scattering contribution was introduced by impurity scattering, which is consistent with the case of Fe-doped $\text{Co}_3\text{Sn}_2\text{S}_2$ bulks (Supplementary Figs. 17 and 18). Owing to the simultaneous increase in ρ_{xx} and σ_H^A , $\tan\theta^A$ increases rapidly, as expected from Fig. 1a,b, Fig. 3e and Table 1 (case III). The measured values are improved by a considerable margin (Fig. 3e,f). A $\tan\theta^A$ value up to 0.46, corresponding to $\theta^A \approx 25^\circ$, is an order of magnitude higher than those of many magnetic materials. The data of zero-field $\tan\theta^A$ from the literature and our results are shown in Fig. 3f (Supplementary Section 4). The $\tan\theta^A$ values of most materials

are below 0.05, which indicates that they are located around the corner of the $\rho_{xx}-\sigma_H^A$ plane (Fig. 3f, purple and blue curves); however, we show a value of 0.46.

Since the first report on θ^A over 70 years ago³⁶, the reported values of θ^A have remained relatively low so far. Enhancements in θ^A were observed with the emergence of magnetic Weyl semimetals (red pentagram) and our scheme now offers higher values of θ^A (red–yellow pentagrams), as shown in Fig. 4a. According to the voltage sensitivity formula of anomalous Hall sensors (Supplementary Equation (9)), a large θ^A value can generate larger voltage changes under the same conditions of longitudinal voltage, saturation field and dimensional ratio of devices, which can intrinsically promote the signal-to-noise performance in key chips against the additional operational amplifiers usually used in sensing circuits. To validate the large θ^A effect, we fabricated anomalous Hall sensors using Fe-doped $\text{Co}_3\text{Sn}_2\text{S}_2$ single-crystalline nanoflakes. The anomalous Hall voltage is utilized to detect the external magnetic field. The magnetic field detectability ($23.5 \pm 1.7 \text{ nT Hz}^{-0.5}$ at 1 Hz) was obtained owing to high sensitivity ($7,028 \pm 341 \mu\text{V cm T}^{-1}$) and low Hall voltage noise (Fig. 4b and Supplementary Fig. 21), exhibiting a competitive advantage compared with the materials used in current anomalous Hall sensors (Fig. 4c).

Conclusions

We have proposed an expression for $\tan\theta^A$ with ρ_{xx} and σ_H^A , and reported the modulation of θ^A . On the basis of this, several design approaches were demonstrated in the magnetic Weyl semimetal $\text{Co}_3\text{Sn}_2\text{S}_2$. We observed a $\tan\theta^A$ value of up to a magnitude of 0.46, corresponding to a θ^A value of around 25° . We also fabricated anomalous Hall sensing devices and demonstrated a sensitivity of $7,028 \pm 341 \mu\text{V cm T}^{-1}$ and a magnetic field detectability of $23.5 \pm 1.7 \text{ nT Hz}^{-0.5}$ at 1 Hz. Our scheme could potentially be used to modulate giant anomalous Hall currents and even giant spin Hall currents in other topological magnets^{37,38}. Our approach could also help in the development of devices based on emerging topological materials for applications in magneto-electronics and spintronics^{39–41}, such as automatic intelligent vehicles and hard-disc readers⁸.

Methods

Crystal growth and device fabrication

The $\text{Co}_3\text{Sn}_2\text{S}_2$ single-crystalline bulks were grown by self-flux methods with Sn flux. High-purity Co (99.98%), Sn (99.999%) and S (99.99%) were put into an alumina crucible and sealed into a high-vacuum quartz tube to prevent oxidation at high temperatures. The samples were heated to $1,050^\circ\text{C}$ and kept for 24 h, and then cooled to 700°C for centrifugation. The compositions of $\text{Co}_3\text{Sn}_2\text{S}_2$ single crystals were checked by energy-dispersive X-ray spectroscopy. The crystal structure was characterized by X-ray diffraction at room temperature, which indicates that the grown crystals have good quality (Supplementary Fig. 8). The structural analysis indicates the space group of $R\bar{3}m$ (no. 166) for $\text{Co}_3\text{Sn}_2\text{S}_2$, in which Co_3Sn forms a quasi-two-dimensional lattice, forming a sandwich structure with S atoms.

Pristine and Fe-doped $\text{Co}_3\text{Sn}_2\text{S}_2$ single-crystalline nanoflakes were grown on Al_2O_3 substrates by the chemical vapour transport method. The polycrystalline raw material and transport agent were sealed into a quartz tube in a high vacuum to grow single-crystal nanoflakes under different temperature gradients. Hexagonal flakes with diameters of $\sim 10\text{--}100 \mu\text{m}$ and thicknesses of $\sim 10\text{--}100 \text{ nm}$ were obtained. Atomic force microscopy was used to characterize the thickness of the nanoflakes. The $\text{Co}_3\text{Sn}_2\text{S}_2$ nanoflakes have good regular morphology (Supplementary Fig. 13), which makes it easy to fabricate the Hall bar pattern along the a axis on the sample (Supplementary Fig. 9). Electron-beam lithography and ion-beam etching were used to fabricate the Hall bar geometry devices. Electron-beam evaporation was used to evaporate the electrodes (Ti and Au).

Magnetization measurements

A Quantum Design vibrating sample magnetometer based on the physical property measurement system (PPMS) was used to measure the magnetization of $\text{Co}_3\text{Sn}_2\text{S}_2$ bulks. Standard samples were prepared for magnetic measurements. The temperature-dependent magnetization from 2 K to 300 K with the magnetic field direction along the c axis is shown in Fig. 3a.

The magnetization of $\text{Co}_3\text{Sn}_2\text{S}_2$ nanoflake was measured by the diamond nitrogen-vacancy (NV) centres. Nanodiamonds with ensemble NV centres (Adamas Nanotechnologies; NV concentration, $\sim 3 \text{ ppm}$; nanodiamond diameter, $\sim 100 \text{ nm}$) were dropped onto the surface of the $\text{Co}_3\text{Sn}_2\text{S}_2$ nanoflakes (Supplementary Fig. 15c). The sample was then loaded into a closed-cycle optical cryostat (Montana Instruments S100) for low-temperature measurements. Optically detected magnetic resonance spectra were obtained for each selected nanodiamond by recording their NV fluorescence and simultaneously scanning the frequency of the applied microwave signal. These spectra were fitted with a multipeak Lorentz function and the splitting between the outermost resonant dips was used to estimate the magnetic field strength (Supplementary Fig. 15d and Fig. 3a).

Transport measurements

The $\text{Co}_3\text{Sn}_2\text{S}_2$ single-crystalline bulks were prepared in long strips for electronic transport measurements, which were performed on the PPMS resistivity option. The transport measurements of nanoflakes were performed using the Quantum Design PPMS, Keithley 2400 and Keithley 2182A. The linear I – V curves were confirmed before the measurements. In all the electrical transport measurements, the current is along the x (a) axis ($[2\bar{1}10]$), the Hall measurements are along the y axis ($[01\bar{1}0]$) and the magnetic field is parallel to the z (c) axis ($[0001]$) (Supplementary Fig. 9). All the measurement results of the longitudinal (transverse) resistance were symmetrized (anti-symmetrized).

Anomalous Hall sensing measurements

The low-temperature environment for anomalous Hall sensing measurements is provided by PPMS. The alternating current with an effective value of 1 mA was applied in the x direction of the sample as the driving current, which was generated by a lock-in amplifier (Zurich Instruments, MFLI). The transverse (y -axis) anomalous Hall voltage was measured by the lock-in amplifier (x and y axes are shown in Supplementary Fig. 20). Then, the periodogram was used to estimate the power spectral density of anomalous Hall voltage (S_V). Repeated anomalous Hall voltage measurements were performed to obtain the expectation of S_V . The magnetic field detectability $S_T^{0.5}$ can be calculated by $S_T^{0.5} = S_V^{0.5}/I_s$, where I_s is the driving current, $s = \Delta R^A/\Delta(\mu_0 H)$ and R^A is the anomalous Hall resistance.

Data availability

The data that support the findings of this study are available from the corresponding author upon reasonable request. Source data are provided with this paper.

References

- Nagaosa, N., Sinova, J., Onoda, S., MacDonald, A. H. & Ong, N. P. Anomalous Hall effect. *Rev. Mod. Phys.* **82**, 1539–1592 (2010).
- Berger, L. Side-jump mechanism for the Hall effect of ferromagnets. *Phys. Rev. B* **2**, 4559–4566 (1970).
- Xiao, D., Chang, M.-C. & Niu, Q. Berry phase effects on electronic properties. *Rev. Mod. Phys.* **82**, 1959–2007 (2010).
- Ihama, S. et al. Spin-transfer torque induced by the spin anomalous Hall effect. *Nat. Electron.* **1**, 120–123 (2018).
- Gibbons, J. D., MacNeill, D., Buhrman, R. A. & Ralph, D. C. Reorientable spin direction for spin current produced by the anomalous Hall effect. *Phys. Rev. Appl.* **9**, 064033 (2018).

6. Wang, K., Zhang, Y., Zhou, S. & Xiao, G. Micron-scale anomalous Hall sensors based on $\text{Fe}_x\text{Pt}_{1-x}$ thin films with a large Hall angle and near the spin-reorientation transition. *Nanomaterials* **11**, 854 (2021).
7. Wang, K., Zhang, Y. & Xiao, G. Anomalous Hall sensors with high sensitivity and stability based on interlayer exchange-coupled magnetic thin films. *Phys. Rev. Appl.* **13**, 064009 (2020).
8. Nakatani, T. et al. Perspective on nanoscale magnetic sensors using giant anomalous Hall effect in topological magnetic materials for read head application in magnetic recording. *Appl. Phys. Lett.* **124**, 070501 (2024).
9. Liu, E. K. et al. Giant anomalous Hall effect in a ferromagnetic kagome-lattice semimetal. *Nat. Phys.* **14**, 1125–1131 (2018).
10. Li, P. et al. Giant room temperature anomalous Hall effect and tunable topology in a ferromagnetic topological semimetal Co_2MnAl . *Nat. Commun.* **11**, 3476 (2020).
11. Belopolski, I. et al. Discovery of topological Weyl fermion lines and drumhead surface states in a room temperature magnet. *Science* **365**, 1278–1281 (2019).
12. Shen, J. et al. Magnetic-field modulation of topological electronic state and emergent magneto-transport in a magnetic Weyl semimetal. *Innovation (Camb.)* **4**, 100399 (2023).
13. Shen, J. et al. Local disorder-induced elevation of intrinsic anomalous Hall conductance in an electron-doped magnetic Weyl semimetal. *Phys. Rev. Lett.* **125**, 086602 (2020).
14. Shen, J. et al. 33% giant anomalous Hall current driven by both intrinsic and extrinsic contributions in magnetic Weyl semimetal $\text{Co}_3\text{Sn}_2\text{S}_2$. *Adv. Funct. Mater.* **30**, 2000830 (2020).
15. Shen, J. et al. Intrinsically enhanced anomalous Hall conductivity and Hall angle in Sb-doped magnetic Weyl semimetal $\text{Co}_3\text{Sn}_2\text{S}_2$. *APL Mater.* **10**, 090705 (2022).
16. Tian, Y., Ye, L. & Jin, X. Proper scaling of the anomalous Hall effect. *Phys. Rev. Lett.* **103**, 087206 (2009).
17. Hou, D. et al. Multivariable scaling for the anomalous Hall effect. *Phys. Rev. Lett.* **114**, 217203 (2015).
18. Chang, C. Z. et al. Experimental observation of the quantum anomalous Hall effect in a magnetic topological insulator. *Science* **340**, 167–170 (2013).
19. Yang, S. Y. et al. Giant, unconventional anomalous Hall effect in the metallic frustrated magnet candidate, KV_3Sb_5 . *Sci. Adv.* **6**, eabb6003 (2020).
20. Miyasato, T. et al. Crossover behavior of the anomalous Hall effect and anomalous Nernst effect in itinerant ferromagnets. *Phys. Rev. Lett.* **99**, 086602 (2007).
21. Onoda, S., Sugimoto, N. & Nagaosa, N. Quantum transport theory of anomalous electric, thermoelectric, and thermal Hall effects in ferromagnets. *Phys. Rev. B* **77**, 165103 (2008).
22. Onoda, S., Sugimoto, N. & Nagaosa, N. Intrinsic versus extrinsic anomalous Hall effect in ferromagnets. *Phys. Rev. Lett.* **97**, 126602 (2006).
23. Liu, D. F. et al. Magnetic Weyl semimetal phase in a kagomé crystal. *Science* **365**, 1282 (2019).
24. Deng, Y. et al. Quantum anomalous Hall effect in intrinsic magnetic topological insulator MnBi_2Te_4 . *Science* **367**, 895 (2020).
25. Zhang, S. et al. Scaling of Berry-curvature monopole dominated large linear positive magnetoresistance. *Proc. Natl Acad. Sci. USA* **119**, e2208505119 (2022).
26. Ikeda, J. et al. Critical thickness for the emergence of Weyl features in $\text{Co}_3\text{Sn}_2\text{S}_2$ thin films. *Commun. Mater.* **2**, 18 (2021).
27. Wieder, H. H. Thickness dependence of electron mobility of InSb films. *J. Vac. Sci. Technol.* **9**, 1193–1196 (1972).
28. Kaveh, M. & Wiser, N. Electron-electron scattering in conducting materials. *Adv. Phys.* **33**, 257–372 (2006).
29. Yeh, S. S., Lin, J. J., Xiunian, J. & Dianlin, Z. Electron-phonon-impurity interference effect in disordered $\text{Au}_{56}\text{Pd}_{44}$ and IrO_2 thick films. *Phys. Rev. B* **72**, 024204 (2005).
30. Mathon, J. & Wohlfarth, E. P. Temperature dependence of the spin-wave energy in the itinerant electron model of ferromagnetism. *J. Appl. Phys.* **39**, 475–475 (1968).
31. Wang, Q. et al. Large intrinsic anomalous Hall effect in half-metallic ferromagnet $\text{Co}_3\text{Sn}_2\text{S}_2$ with magnetic Weyl fermions. *Nat. Commun.* **9**, 3681 (2018).
32. Guguchia, Z. et al. Tunable anomalous Hall conductivity through volume-wise magnetic competition in a topological kagome magnet. *Nat. Commun.* **11**, 559 (2020).
33. Liu, D. F. et al. Topological phase transition in a magnetic Weyl semimetal. *Phys. Rev. B* **104**, 205140 (2021).
34. Liu, C. et al. Spin excitations and spin wave gap in the ferromagnetic Weyl semimetal $\text{Co}_3\text{Sn}_2\text{S}_2$. *Sci. China Phys., Mech. Astron.* **64**, 217062 (2020).
35. Rathod, S., Malasi, M., Lakhani, A. & Kumar, D. Electron-magnon scattering in an anisotropic half-metallic ferromagnetic Weyl semimetal $\text{Co}_3\text{Sn}_2\text{S}_2$. *Phys. Rev. Mater.* **6**, 084202 (2022).
36. Smit, J. & Volger, J. Spontaneous Hall effect in ferromagnetics. *Phys. Rev.* **92**, 1576–1577 (1953).
37. Sinova, J. et al. Spin Hall effects. *Rev. Mod. Phys.* **87**, 1213–1260 (2015).
38. Derunova, E. et al. Giant intrinsic spin Hall effect in W_3Ta and other A15 superconductors. *Sci. Adv.* **5**, eaav8575 (2019).
39. Tokura, Y., Yasuda, K. & Tsukazaki, A. Magnetic topological insulators. *Nat. Rev. Phys.* **1**, 126–143 (2019).
40. Yang, S.-H., Naaman, R., Paltiel, Y. & Parkin, S. S. P. Chiral spintronics. *Nat. Rev. Phys.* **3**, 328–343 (2021).
41. He, Q. L. et al. Topological spintronics and magnetoelectronics. *Nat. Mater.* **21**, 15–23 (2021).
42. Zhang, Y., Hao, Q. & Xiao, G. Low-frequency noise of magnetic sensors based on the anomalous Hall effect in Fe-Pt alloys. *Sensors* **19**, 3537 (2019).
43. Zhang, Y., Wang, K. & Xiao, G. Noise characterization of ultrasensitive anomalous Hall effect sensors based on $\text{Co}_{40}\text{Fe}_{40}\text{B}_{20}$ thin films with compensated in-plane and perpendicular magnetic anisotropies. *Appl. Phys. Lett.* **116**, 212404 (2020).

Acknowledgements

We thank B. Yan for valuable discussions. This work was supported by the State Key Development Program for Basic Research of China (no. 2022YFA1403800, to B.W.), the National Natural Science Foundation of China (no. 11974394, to E.L.; no. 12174426, to H.W.), the CAS Project for Young Scientists in Basic Research YSBR- 057 (to M.L.), the Strategic Priority Research Program (B) of the Chinese Academy of Sciences (CAS) (no. XDB33000000, to E.L.), the Synergetic Extreme Condition User Facility (SECUF, to E.L.) and the Scientific Instrument Developing Project of CAS (no. ZDKYYQ20210003, to E.L.).

Author contributions

E.L. conceived and supervised the project. X.D. and M.L. synthesized the $\text{Co}_3\text{Sn}_2\text{S}_2$ bulks. J.Y., Q.Z. and S.Z. grew the nanoflakes. J.Y., Y. Wang and Y.L. carried out the X-ray diffraction measurements. J.Y. and Y. Wang performed the magnetic measurements of the bulks using a vibrating sample magnetometer. Y.S. and G.L. performed the magnetic measurements of the nanoflakes by NV centres. J.Y. and X.L. performed the fabrication of Hall devices and the measurements of anomalous Hall sensing. J.Y., B.W., H.W., Y. Wu, S.P., G.L., C.F., E.L. and B.S. analysed and discussed the experimental data. J.Y. and E.L. wrote this manuscript with input from all authors.

Competing interests

The authors have applied for a Chinese patent (no. 2025101128621) for anomalous Hall sensors based on a large anomalous Hall angle and their preparation methods, which is now under consideration.

Additional information

Supplementary information The online version contains supplementary material available at <https://doi.org/10.1038/s41928-025-01364-8>.

Correspondence and requests for materials should be addressed to Enke Liu.

Peer review information *Nature Electronics* thanks the anonymous reviewers for their contribution to the peer review of this work.

Reprints and permissions information is available at www.nature.com/reprints.

Publisher's note Springer Nature remains neutral with regard to jurisdictional claims in published maps and institutional affiliations.

Springer Nature or its licensor (e.g. a society or other partner) holds exclusive rights to this article under a publishing agreement with the author(s) or other rightsholder(s); author self-archiving of the accepted manuscript version of this article is solely governed by the terms of such publishing agreement and applicable law.

© The Author(s), under exclusive licence to Springer Nature Limited 2025